Chemical Science

ROYAL SOCIETY OF CHEMISTRY

EDGE ARTICLE

View Article Online
View Journal | View Issue

Cite this: *Chem. Sci.*, 2023, **14**, 12056

All publication charges for this article have been paid for by the Royal Society of Chemistry

Received 8th August 2023
Accepted 12th October 2023

DOI: 10.1039/d3sc04135b

rsc.li/chemical-science

Water sensitivity of heteroepitaxial Cu-MOF films: dissolution and re-crystallization of 3D-oriented MOF superstructures†

Lea A. Brandner, [a] Mercedes Linares-Moreau, [a] Guojun Zhou, [b] Heinz Amenitsch, [c] Simone Dal Zilio, [d] Zhehao Huang, [b] Christian Doonan *[e] and Paolo Falcaro *[a]

3D-oriented metal–organic framework (MOF) films and patterns have recently emerged as promising platforms for sensing and photonic applications. These oriented polycrystalline materials are typically prepared by heteroepitaxial growth from aligned inorganic nanostructures and display anisotropic functional properties, such as guest molecule alignment and polarized fluorescence. However, to identify suitable conditions for the integration of these 3D-oriented MOF superstructures into functional devices, the effect of water (gaseous and liquid) on different frameworks should be determined. We note that the hydrolytic stability of these heteroepitaxially grown MOF films is currently unexplored. In this work, we present an in-depth analysis of the structural evolution of aligned 2D and 3D Cu-based MOFs grown from $Cu(OH)_2$ coatings. Specifically, 3D-oriented Cu_2L_2 and Cu_2L_2DABCO films (L = 1,4-benzenedicarboxylate, BDC; biphenyl-4,4-dicarboxylate, BPDC; DABCO = 1,4-diazabicyclo[2.2.2]octane) were exposed to 50% relative humidity (RH), 80% RH and liquid water. The combined use of X-ray diffraction, infrared spectroscopy, and scanning electron microscopy shows that the sensitivity towards humid environments critically depends on the presence of the DABCO pillar ligand. While oriented films of 2D MOF layers stay intact upon exposure to all levels of humidity, hydrolysis of Cu_2L_2DABCO is observed. In addition, we report that in environments with high water content, 3D-oriented $Cu_2(BDC)_2$DABCO recrystallizes as 3D-oriented $Cu_2(BDC)_2$. The heteroepitaxial MOF-to-MOF transformation mechanism was studied with *in situ* synchrotron experiments, time-resolved AFM measurements, and electron diffraction. These findings provide valuable information on the stability of oriented MOF films for their application in functional devices and highlight the potential for the fabrication of 3D-oriented superstructures *via* MOF-to-MOF transformations.

Introduction

Metal–organic frameworks (MOFs) are a class of extended materials consisting of inorganic nodes and multitopic organic ligands.[1,2] By carefully selecting their organic and inorganic components the physical and structural properties of MOFs can be customized.[3] The control over chemical and structural properties enables the preparation of MOFs with relevant electric,[4] magnetic[5] and optical[6] functionalities. Furthermore, advances in fabrication protocols have enabled the preparation of polycrystalline MOF thin films and patterns[7–10] and the potential to exploit such MOF properties in devices.[11–13] Recent progress in the fabrication of MOF devices focused on the control over directional functional properties (*i.e.* anisotropic properties); for this, fabrication protocols affording precise alignment of individual porous crystals are required.[14,15] In this context, precisely oriented polycrystalline systems have been recently reported.[16–18] In particular, 3D-oriented MOF films and patterns have been prepared from ceramic nanostructures with uniform crystallographic orientation.[19–21] In this process, pre-aligned $Cu(OH)_2$ nanobelts (NBs) are deposited on a solid support; in the presence of alcoholic solutions with suitable dicarboxylic linkers,[22] the NBs act as source of Cu(II) and sacrificial substrate for the epitaxial growth of the MOF coating.[23] The resulting 3D-oriented MOF films, and more recently 3D-oriented micropatterns, exhibit anisotropy-derived properties, such as guest molecule alignment, polarized fluorescence, or polarization-dependent plasmon-resonance, among others.[19,21,24–26]

[a]*Institute of Physical and Theoretical Chemistry, Graz University of Technology, 8010 Graz, Austria. E-mail: paolo.falcaro@tugraz.at*

[b]*Department of Materials and Environmental Chemistry, Stockholm University, Stockholm SE-106 91, Sweden*

[c]*Institute of Inorganic Chemistry, Graz University of Technology, 8010 Graz, Austria*

[d]*CNR-IOM – Istituto Officina dei Materiali, SS 14, km 163.5, Basovizza, Trieste, 34149, Italy*

[e]*Department of Chemistry, The University of Adelaide, Adelaide, South Australia, 5005, Australia. E-mail: christian.doonan@adelaide.edu.au*

† Electronic supplementary information (ESI) available. See DOI: https://doi.org/10.1039/d3sc04135b

An aspect of MOF devices that requires further study is how the material structure changes under typical working conditions, *e.g.* humidity. We hypothesized that the exposure of heteroepitaxially oriented MOF films to humidity could result in chemical and structural changes. In the literature, several Cu-based MOFs were reported to show sensitivity towards water, resulting in degradation of the crystal structure and loss of functional properties.[27–33] For archetypical HKUST-1 ($Cu_3(BTC)_2$, BTC = 1,3,5-benzene tricarboxylate),[34] it has been reported that a relative humidity (RH) above 50% RH results in the decomposition of the framework.[35] Interestingly, for other MOFs (*e.g.* MOF-177), the interaction with water molecules triggers the re-organization of the unit cell into new crystalline phases.[36] Recently, Fu and co-workers reported the epitaxial recrystallization from a single-crystal MOF to an oriented MOF superstructure (*i.e.* an ordered polycrystalline structure).[37] Inspired by these works, we decided to examine the effect of water on heteroepitaxially grown Cu-MOF films. We examined two aspects: (i) the hydrolytic stability of different heteroepitaxially grown Cu-MOF films and (ii) the potential rearrangement of 3D-oriented MOF films into different ordered polycrystalline structures. In particular, in this study, we assess the influence of water on four different oriented Cu-MOF films (Cu_2L_2, Cu_2L_2DABCO, (L = 1,4-benzenedicarboxylate, BDC; biphenyl-4,4-dicarboxylate, BPDC) exposed to varying levels of humidity (Fig. 1). Heteroepitaxial MOF films were grown from sacrificial $Cu(OH)_2$ oriented nanostructures and exposed to 50% RH, 80% RH, and liquid water. Changes in crystallinity, chemical composition, and morphology were monitored over a period of 7 days, using X-ray diffraction (XRD), Fourier-transform infrared spectroscopy (FTIR), and scanning electron microscopy (SEM). While the 2D-frameworks $Cu_2(BDC)_2$ and $Cu_2(BPDC)_2$ maintained their physical and chemical properties in the presence of water, we observed the hydrolysis and concomitant transformation from $Cu_2(BDC)_2$DABCO films to Cu_2BDC_2, as well as structural degradation of $Cu_2(BPDC)_2$DABCO starting from 50% RH. To elucidate the timescale and mechanism of the MOF transformation process, we performed time-resolved grazing incidence wide-angle X-ray scattering (GIWAXS) experiments using synchrotron radiation. These results were also correlated to time-resolved atomic force microscopy (AFM) measurements to study the corresponding changes in morphology and electron diffraction for structural changes. The collected data reveal that, at room-temperature, the MOF transformation process starts with the dissolution of the MOF crystals, then the initial 3D-oriented polycrystalline film undergoes heteroepitaxial recrystallization into a distinct 3D-oriented polycrystalline superstructure. We posit that this study (i) will help the progress of oriented MOF films towards micro- and opto-electronic devices and (ii) will advance the knowledge on ordered polycrystalline MOF superstructures.

Experimental

Materials

1,4-Benzenedicarboxylic acid (H_2BDC), 1,4-diazabicyclo[2.2.2] octane (DABCO), absolute ethanol (EtOH, 99.7%), methanol (MeOH), dichloromethane (DCM), and acetic acid (99%) were purchased from Sigma Aldrich. Biphenyl-4,4-dicarboxylic acid (H_2BPDC) was bought from Tokyo Chemical Industry Co. Ltd. $Cu(OH)_2$ nanobelts (NBs) were prepared and deposited on Si pieces (1.5 × 1.5 cm^2) according to previously reported procedures.[19,23] All reagents were used without further purification.

Characterization

Powder X-ray diffraction patterns were obtained using a Rigaku Smart Lab instrument with CuKα radiation (λ = 0.154 nm). To

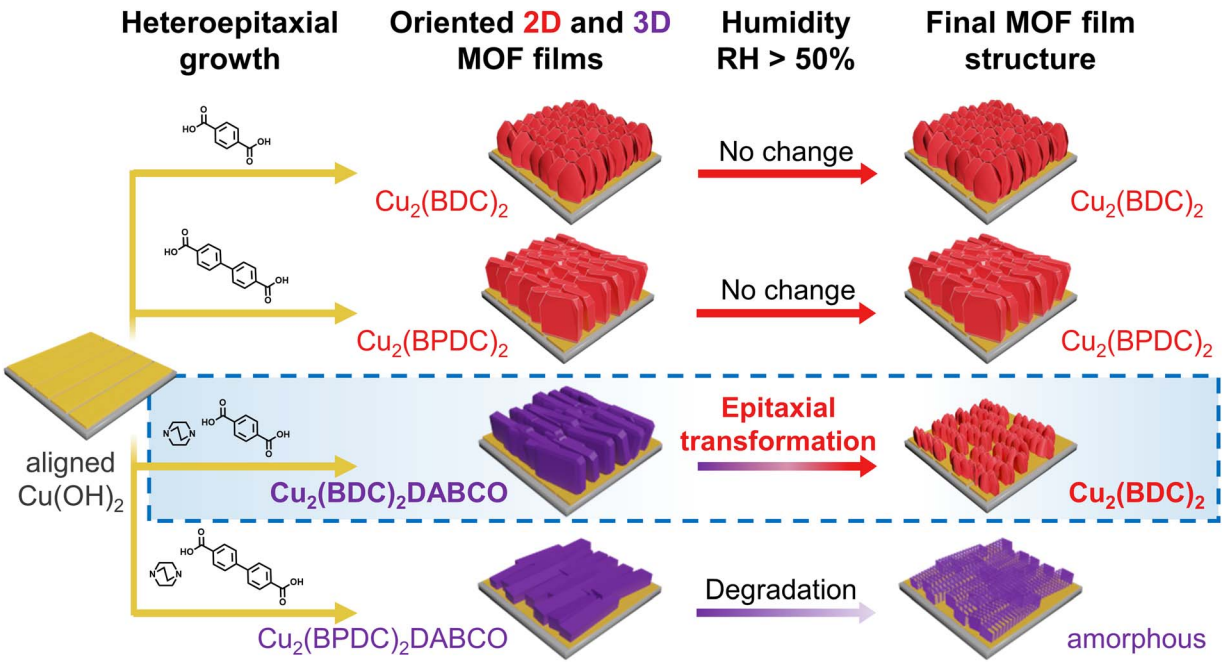

Fig. 1 Schematic illustration of the structural evolution of heteroepitaxially grown, oriented MOF films under humid conditions.

assess the crystalline orientation of the MOFs films, intensity profiles of selected reflections were recorded by azimuthal angle scans in the in-plane XRD configuration. FTIR spectra were recorded in transmission mode using a Bruker ALPHA spectrometer in the 4000–400 cm^{-1} range (average over 32 scans, 4 cm^{-1} spectral resolution). Sample morphologies were imaged by using a ZEISS Sigma 300 FEG scanning electron microscope, equipped with standard SE2 and INLENS detectors. Time-resolved grazing incidence wide-angle X-ray scattering (GIWAXS) measurements were performed at the Austrian SAXS beamline at Elettra Sincrotrone, Trieste, Italy.[38] An X-ray beam with a wavelength of 0.077 nm and a photon energy of 16 keV was used. 2D GIWAXS patterns were recorded with a Pilatus3 1 M detector at a grazing angle of 1°. Silver behenate was used to calibrate the angular scale of the detector. The intensity of the scattered photons was recorded and diffraction patterns parallel (q_y, in-plane cut) and perpendicular (q_z, out-of-plane cut) to the sample surface considered for data analysis. Samples were measured in a q-range of $0.83 < q < 31$ nm^{-1}. The relative humidity (RH) during the SAXS experiments was controlled with a cylindrical metal chamber, equipped with two Kapton windows for passage of the incident and scattered beam (Fig. S1†).[39] RH values were set by mixing different proportions of dry (<3% RH) and humid (>95% RH) air. A humidity sensor combined with a proportional integral derivative (PID) controller was used to tune the humidity inside the chamber. For the experiments performed in H_2O, a customized 3D-printed chemical cell, equipped with two Kapton windows and solvent inlet was used (Fig. S1†).[40] For azimuthal angle scans, samples were mounted on a motorized stage and rotated along the axis normal to the surface. All GIWAXS measurements were conducted at a constant temperature of 25 ± 1 °C. More experimental details are given in the ESI.† Time-resolved AFM measurements were performed using an Oxford Instruments Asylum Cypher ES in blueDrive tapping mode, equipped with BudgetSensors Tap300 silicon cantilevers. The measurements were performed inside a closed environmental control cell. Initially, a flow of dry Ar was used for calibration of the measurement parameters. Then, the dry Ar flow was exchanged with a humid Ar flow (80% RH measured at the exit of the chamber). Scans were collected continuously at a scan rate of 9 Hz. When comparing the GIWAXS and the AFM setups, it is worth noting that the different setups (*e.g.* different fluxes and volume of humid air in the reaction chambers) resulted in slightly different kinetics. Transmission electron microscope (TEM) data was obtained on a JEOL JEM2100 microscope, which was operated at 200 kV (Cs 1.0 mm, point resolution 0.23 nm). Images were recorded with a Gatan Orius 833 CCD camera (resolution 2048 × 2048 pixels, pixel size 7.4 μm). Electron diffraction patterns were recorded with a Timepix pixel detector QTPX-262k (512 × 512 pixels, pixel size 55 μm, Amsterdam Sci. Ins.).

Synthesis of pristine MOF films Cu_2L_2. The oriented Cu_2L_2 MOF films were prepared according to a literature procedure.[19] In short, the aligned $Cu(OH)_2$ nanobelt films were immersed in a conversion solution (3.6 mL of DI H_2O, 9.34 mL of ethanol, 0.01 g of ligand) and left standing at RT (23 °C) for 30 min (H_2BDC) or 1 h (H_2BPDC). Afterwards, the films were removed, thoroughly rinsed with absolute EtOH, and dried under N_2 flow.

Synthesis of pristine MOF films $Cu_2(BDC)_2DABCO$. Oriented $Cu_2(BDC)_2DABCO$ films were prepared following a previously reported protocol.[21] In short, the oriented $Cu(OH)_2$ substrates were immersed in a converting solution of H_2BDC (11.0 mg, 6.64 mM) and DABCO (30 mg, 26.7 mM) in 10 mL of MeOH. After leaving the closed vials in an oven at 70 °C for 1 h, the films were removed, gently rinsed with absolute EtOH, and dried under N_2 flow.

Synthesis of pristine MOF films $Cu_2(BPDC)_2DABCO$. Oriented $Cu_2(BPDC)_2DABCO$ films were prepared adapting a literature procedure:[20] oriented $Cu(OH)_2$ coatings were immersed in 2 mL of a pre-prepared methanolic solution of H_2BPDC (4 mM), DABCO (256 mM), and acetic acid (35 mM). After leaving the films in a closed vial in an oven at 60 °C for 1.5 h, the converted samples were removed, gently rinsed with absolute EtOH, and dried under N_2 flow.

Exposure to humidity. After synthesis, triplicates of pristine MOF films were stored inside humidity chambers ($V = 1$ dm^3), equipped with a humidity sensor, and kept at 50% RH and 80% RH. Films exposed to water were kept in separate and closed vials with 2 mL DI H_2O. The films were removed from the humid environments after 1, 3 and 7 days for *ca.* 10 min to perform FTIR and XRD characterization (FTIR spectra and XRD patterns recorded at 30–40% RH). Films for SEM characterization were removed after selected time-points, solvent-exchanged to DCM (3 × 10 min), evacuated for 30 min and stored under inert conditions (*i.e.* Ar atmosphere).

Results and discussion

Understanding structural changes in 3D-oriented MOF films under various environmental conditions, particularly different RH, is crucial for the successful implementation of these materials into functional devices. For example, optical components that are susceptible to change of properties because of humidity require encasing. To evaluate potential humidity values for our initial tests, we note that RH = 50% aligns with the upper limit of relative humidity recommended by the FDA for laboratory settings, and falls within the optimal range of 30–60% RH, which is considered ideal for human health in indoor environments.[41] Therefore, we chose 50% RH as a reasonable environmental condition to simulate the handling of these components and their indoor use. In order to further understand the interaction between water and the heteroepitaxially grown MOF films, including potential degradation processes, we also explored higher humidity values including 80% RH and liquid water as extreme testing conditions. The oriented MOF films were prepared from aligned $Cu(OH)_2$ NBs on Si substrates *via* previously reported literature protocols and outlined as follows.[19–21] For the synthesis of $Cu_2(BDC)_2$ and $Cu_2(BPDC)_2$ films, oriented $Cu(OH)_2$ NBs substrates were immersed in ethanol/water mixtures, containing H_2BDC or H_2BPDC, and reacted for 30 min (H_2BDC) and 1 h (H_2BPDC) at room temperature. $Cu_2(BDC)_2DABCO$ and $Cu_2(BPDC)_2DABCO$ films were grown from $Cu(OH)_2$ templates in methanolic solutions of

the corresponding organic linker and DABCO for 1 h (70 °C, H_2BDC, DABCO) and 1.5 h (60 °C, H_2BPDC, DABCO), respectively. For each type of heteroepitaxially grown MOF film, a set of triplicate samples was placed in humidity-controlled chambers set at 50% RH and 80% RH, and immersed in DI water. To assess changes in crystallinity, chemical composition and morphology, we examined the MOF films by using X-ray diffraction (XRD), Fourier-transform infrared spectroscopy (FTIR), and scanning electron microscopy (SEM). After characterization of the as-synthesized samples, the films were analysed after 1, 3, and 7 days. The recorded diffraction patterns were baseline-corrected and the dominant MOF reflection integrated. To capture the structural change for each film and minimize fluctuations related to variations in the mass of crystalline material across samples, each sample was compared to itself: the peak area of the as-synthesized sample was set to 100% and the change in signal monitored over the 7 d. Average and standard deviation of the recorded peak areas in % were calculated for each condition from the set of triplicate samples.

For the as-synthesized MOF films, diffraction plots (Fig. 2a) were consistent with those reported in the literature. Specifically, we observed diffraction peaks at different angles: 8.38°, assigned to the (001) plane of $Cu_2(BDC)_2$;[19] 5.93°, assigned to the (001) plane of $Cu_2(BPDC)_2$;[19] 8.16°, assigned to the (010) plane of $Cu_2(BDC)_2$DABCO;[20,21] and 5.85°, assigned to the (010) plane of $Cu_2(BPDC)_2$DABCO.[20] Azimuthal intensity in-plane XRD-scans confirmed the successful growth of the oriented MOF films (Fig. S2†). Reflections of residual $Cu(OH)_2$ at 16.74° and 23.83°, assigned to the (020) and (021) planes, were also observed for $Cu_2(BDC)_2$, $Cu_2(BPDC)_2$, and $Cu_2(BDC)_2$DABCO in the out-of-plane XRD patterns. For $Cu_2(BPDC)_2$DABCO, these signals were absent in the diffraction pattern, indicating full consumption of the sacrificial $Cu(OH)_2$ NBs. Next, we analysed the diffraction patterns of the films exposed to the different RH values. For the heteroepitaxially grown 2D frameworks $Cu_2(BDC)_2$ and $Cu_2(BDPC)_2$, the peak areas associated with the respective (001) reflections changed within 10–15% of the original signals under all tested conditions (Fig. 2b, c and S3†). It is noteworthy that the error bars overlap for all data points; this excludes significant changes in crystallinity with increasing RH and exposure time. In contrast, we found a significant decrease in signal intensity for $Cu_2(BDC)_2$DABCO and $Cu_2(BPDC)_2$DABCO films after exposure to the different humid environments (Fig. 2d and e). For $Cu_2(BDC)_2$DABCO, the peak areas assigned to the (010) reflection decreased by 90% after exposure to 50% RH for 1 d. In addition, the peak position shifts from 8.16° to 8.27° (Fig. S4†). Interestingly, at 80% RH and in water, the peak area stabilized at approximately 15–18% of the original value, but displayed an even larger shift to 8.37° (Fig. S5†), which is consistent with the (001) reflection of $Cu_2(BDC)_2$. It was also observed that for $Cu_2(BDC)_2$DABCO films, the diffraction signals associated with the (021) plane of the remaining $Cu(OH)_2$, exhibited similar intensity at 50% RH, but decreased slightly at 80% RH and in water (Fig. S5†). For oriented $Cu_2(BPDC)_2$DABCO films, the peak areas attributed to the signal of the (010) reflection dropped by 75% after the first day under 50% RH, followed by another intensity decrease down to 20% of the original peak area after 7 d (Fig. S6†). At 80% RH and in water the integrated peak areas dropped by over 90% within 24 h, indicating almost complete loss of crystallinity (Fig. S6†).

Next, we analysed the chemical changes in the different MOF films by monitoring characteristic vibrational modes over time at the different RH values. We focused on the asymmetric and symmetric carboxylate stretching modes and compared to the pristine samples and previously reported

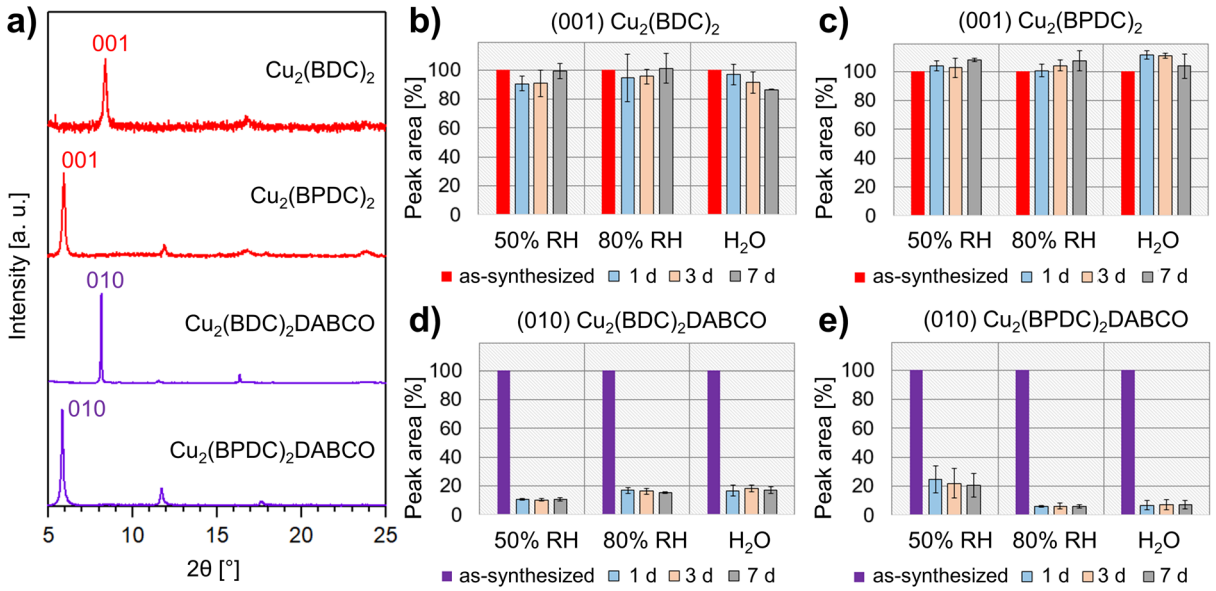

Fig. 2 (a) PXRD patterns of pristine oriented MOF films; (b–e) integrated areas of the dominant MOF reflections: peak areas were set to 100% for the as-synthesized films, then the average peak areas (in %) were calculated from the three replicate samples after exposure to 50% RH, 80% RH, and liquid H_2O for 1, 3 and 7 days.

spectra[23,24,42] to determine the coordination and protonation state of the carboxylic ligands. For the as-synthesized $Cu_2(BDC)_2$ films, the asymmetric and symmetric carboxylate stretching modes were observed at 1579 cm^{-1} and 1398 cm^{-1}, respectively. For pristine $Cu_2(BPDC)_2$, the corresponding vibrational bands appeared at 1583 cm^{-1} and 1423 cm^{-1}. In the case of $Cu_2(BDC)_2DABCO$, we recorded absorption bands at 1630 cm^{-1}, assigned to $\nu_{asymm}(COO^-)$, and overlapping signals at 1433 cm^{-1} and 1394 cm^{-1}, associated with the $\nu_{symm}(COO^-)$ vibration and a benzene ring mode.[27] As-synthesized $Cu_2(BPDC)_2DABCO$ films exhibited an asymmetric carboxylate stretching mode at 1623 cm^{-1} and a broad band at 1406 cm^{-1}, assigned to $\nu_{symm}(COO^-)$.

During the exposure period of 7 days, the vibrational modes of $Cu_2(BDC)_2$ and $Cu_2(BPDC)_2$ preserved both intensity and position; no additional bands appeared in the spectra for all tested conditions (Fig. S7†). These data indicate the negligible influence of water on the chemical composition of the samples. For the $Cu_2(BDC)_2DABCO$ films, the IR spectra revealed several changes induced by humid conditions. After exposure to 50% RH for 1 d, the carboxylate modes lost approximately half their intensity, indicating a substantial degradation of the sample. Additionally, a new vibrational band appeared at 1579 cm^{-1}; this mode could be ascribed to asymmetric carboxylate stretching of $Cu_2(BDC)_2$ (Fig. S8†). Vibrational modes attributed to the DABCO pillar ligand in the region at 2960 cm^{-1} (in-phase $\nu_{asymm}(CH_2)$), at 1318 cm^{-1} (in-phase $\gamma_{twist}(CH_2)$, in-phase $\nu_{asymm}(NC_3)$) and at 1060 cm^{-1} (in-phase $\nu_{asymm}(NC_3)$, ν_{asymm}(-C–C), $\gamma_{twist}(CH_2)$) were also observed[43] and showed only a minimal change in intensity when exposed to 50% RH over time (Fig. S9†). Similar changes in the spectra were observed for $Cu_2(BDC)_2DABCO$ films exposed to 80% RH and water; however, in these samples, the initial asymmetric COO^- band disappeared completely, resulting in carboxylate modes consistent with pure $Cu_2(BDC)_2$ MOF (Fig. S8†). Additionally, the vibrational bands attributed to DABCO disappeared in water, indicating the removal of the pillar ligand from the framework (Fig. S9†). At 80% RH, the intensity of the DABCO-related band at 1060 cm^{-1} decreased over time and Raman maps suggest that DABCO molecules rearrange and aggregate in different regions of the film surface (Fig. S10†). For $Cu_2(BPDC)_2DABCO$ films, a similar drop in intensity of the asymmetric carboxylate stretching vibration was observed within the first 24 h at 50% RH. At the same time, new bands at 1586 cm^{-1} and 1540 cm^{-1} emerged, matching the vibrational modes of $Cu_2(BPDC)_2$ (Fig. S11†). At 80% RH and in water, the asymmetric COO^- mode of the initial framework disappeared completely and only the vibrational signals similar to $Cu_2(BPDC)_2$ remained (Fig. S11†). While the in-phase $\nu_{asymm}(CH_2)$ mode of the DABCO shows little intensity for as-synthesized and exposed films, the vibrational bands at 1318 cm^{-1} and 1060 cm^{-1} are stable at 50% RH, but disappear at high water loading, similar to the observations for $Cu_2(BDC)_2DABCO$ (Fig. S12†).

To correlate the changes observed in the XRD patterns and FTIR spectra with changes of the films' morphologies, we examined the samples as-synthesized and after exposure to the different environments, using scanning electron microscopy (SEM). Pristine films of the 2D frameworks $Cu_2(BDC)_2$ and $Cu_2(BPDC)_2$ showed small, plate-like crystals with diameters of approximately 150 nm (Fig. 3a and b). In contrast to this, micrographs of $Cu_2(BDC)_2DABCO$ films revealed partially intergrown, cuboid crystals, with an average length of 600 nm and width in the 150–400 nm range (Fig. 3c). Pristine Cu_2(-$BPDC)_2DABCO$ films also exhibited a cuboid morphology with crystal lengths up to 2.2 μm and an average width of 500 nm (Fig. 3d). These morphologies are comparable with previous reports of heteroepitaxially grown Cu-MOF films from $Cu(OH)_2$ substrates.[19–21]

When compared to the micrographs of as-synthesized samples, the morphologies of $Cu_2(BDC)_2$ and $Cu_2(BPDC)_2$ exposed to different RH values remain unchanged (Fig. 3e, f, S13 and S14†) indicating minimal impact of humidity and water on the 2D-layered MOF crystal shapes. However, significant changes were observed in the case of $Cu_2(BDC)_2DABCO$. After 7 days at 50% RH, the original large cuboid crystals are replaced by small plate-like crystals (Fig. 3g and S15†). We note that the

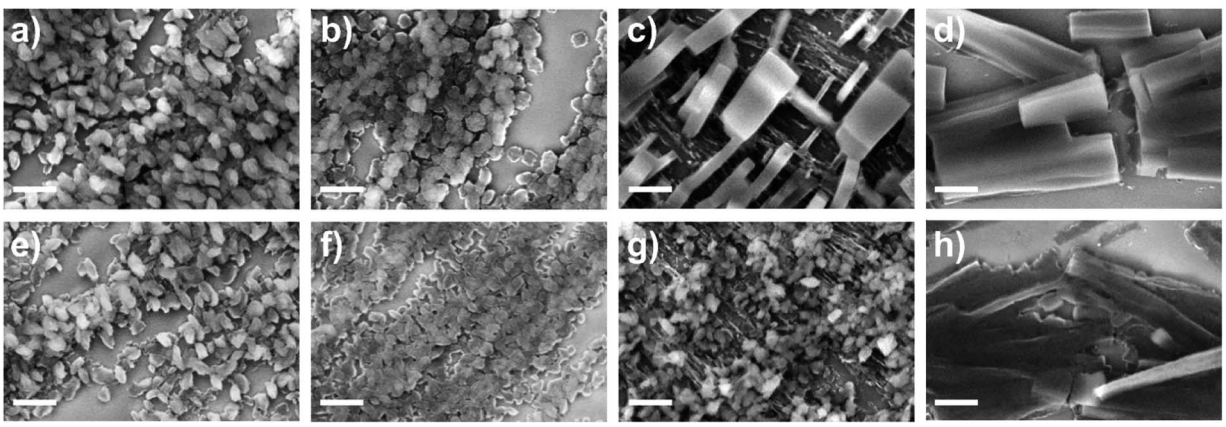

Fig. 3 SEM micrographs of heteroepitaxially grown films, pristine: (a) $Cu_2(BDC)_2$ (2D MOF), (b) $Cu_2(BPDC)_2$ (2D MOF), (c) $Cu_2(BDC)_2DABCO$ (3D MOF), (d) $Cu_2(BPDC)_2DABCO$ (3D MOF); and after exposure to 50% RH for 7 days: (e) $Cu_2(BDC)_2$, (f) $Cu_2(BPDC)_2$, (g) $Cu_2(BDC)_2DABCO$, (h) $Cu_2(BPDC)_2DABCO$. Scale bars of 500 nm for all images.

new crystalline morphology is similar to the one of $Cu_2(BDC)_2$ MOFs (Fig. 3a and e). At higher water loadings, the transformation from a cuboid to a plate-like morphology occurs at a faster rate (*e.g.* < 1 d at 80% RH and in H_2O). These observations suggest the transformation from $Cu_2(BDC)_2DABCO$ to $Cu_2(BDC)_2$.

For $Cu_2(BPDC)_2DABCO$, the overall cuboid crystal shapes remained prominent after the 7 d exposure to 50% RH, but less defined crystal edges and increased surface roughness were observed (Fig. 3h). Under high humidity conditions, individual crystals became gradually more difficult to distinguish and micrographs show holes covering the surface of the remaining material (Fig. S16†).

Structural analysis of the 3D-oriented MOF films after exposure to humid environments

It has been shown in the literature that exposure of $Cu_2(BDC)_2DABCO$ to 50% RH resulted in reduced Cu–Cu interaction, the formation of a Cu–OH moiety and protonation of the carboxylate linkers.[27] An effective hydrolysis of the coordination bonds requires the accumulation of a certain amount of water in the pores, similar to capillary condensation.[44] Consequently, for MOFs with larger voids, a higher partial water pressure is required to facilitate the displacement of the organic linkers. Based on this premise, the MOF films containing BDC with pore channels of 7.5 Å are expected to be more sensitive towards water than their BPDC counterparts, which exhibit wider pores of 10.8 Å.[21,45] Additionally, the access to the MOF voids through suitable pore apertures must also be considered. In the case of heteroepitaxially grown $Cu_2(BDC)_2$ and $Cu_2(BPDC)_2$ films, the 2D MOF layers are closely spaced by 5.8 Å,[19] resulting in small hydrophobic pore openings perpendicular to the substrate surface (Fig. 4a). In contrast, for the pillar-layered 3D MOF films, $Cu_2(BDC)_2DABCO$ and $Cu_2(BPDC)_2DABCO$, the stacking distance is increased to 9.63 Å (Fig. 4b).[19,20] Studies by Fischer and co-workers showed that for layer-by-layer grown SURMOFs, adsorption rates are significantly higher when the MOF voids could be accessed through apertures perpendicular to the substrate surface, while in-plane pore channels with limited out-of-plane access points resulted in lower adsorption rates, especially in densely packed films.[46] Based on these studies, we expected a lower hydrolytic sensitivity for heteroepitaxial 2D MOF films and higher sensitivity for heteroepitaxial 3D MOF films (*i.e.* those containing DABCO).

Our experimental results show that humidity has negligible effects on the crystallinity, chemical composition and morphology of heteroepitaxially grown $Cu_2(BDC)_2$ and $Cu_2(BPDC)_2$ films. Thus, these oriented 2D Cu-MOF frameworks are structurally stable even in highly humid environments. The similar behaviour observed for both linkers (BDC and BPDC) suggests that for these MOFs, the small hydrophobic pore windows prevent an effective mass transfer of water molecules into the larger in-plane pores. Thus, the MOF crystal orientation

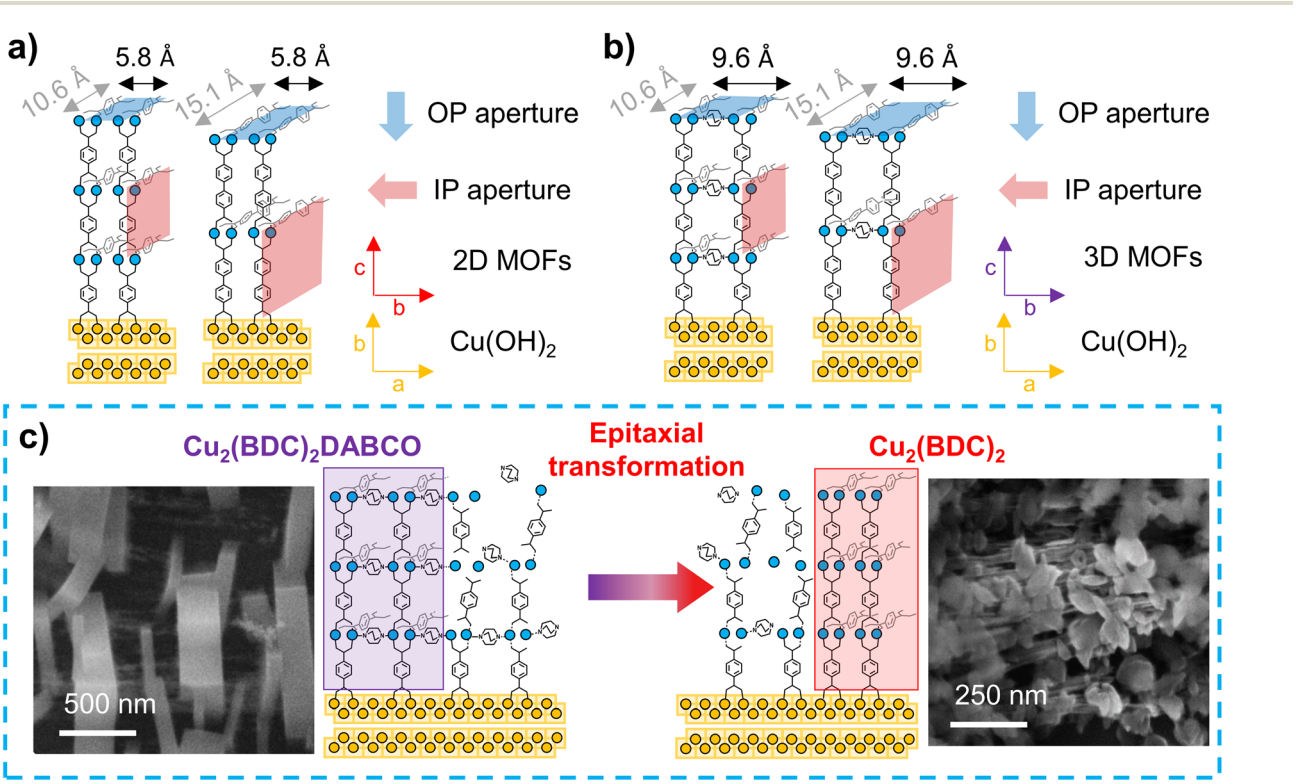

Fig. 4 Schematic of heteroepitaxially grown (a) 2D MOFs ($Cu_2(BDC)_2$, $Cu_2(BPDC)_2$), and (b) 3D MOF ($Cu_2(BDC)_2DABCO$, $Cu_2(BPDC)_2DABCO$) films and their pore windows from out-of-plane (OP, perpendicular to substrate surface) and in-plane (IP, parallel to substrate surface) directions; (c) proposed mechanism for the MOF-to-MOF transformation with SEM micrographs of pristine $Cu_2(BDC)_2DABCO$ film (left), and $Cu_2(BDC)_2$-DABCO film after exposure to liquid H_2O for 1 day (right).

could have a stabilizing contribution. We note that the effect of hydrophobic pore windows was also previously reported for hydrophobic frameworks, which showed a significantly higher affinity towards non-polar molecules over polar guests.[47]

In contrast, in the exposed 3D-oriented $Cu_2(BDC)_2DABCO$ film, reduced crystallinity and decreased intensity of the carboxylate vibrations in the IR spectra are ascribed to the hydrolysis of the framework. In addition, the appearance of new vibrational bands and a plate-like morphology indicate the formation of $Cu_2(BDC)_2$. Although partial decomposition of powdery $Cu_2(BDC)_2DABCO$ at 50% RH has been previously observed,[27] the transformation from 3D-oriented $Cu_2(BDC)_2DABCO$ films to $Cu_2(BDC)_2$ coatings has not been reported to date. In the PXRD patterns recorded of $Cu_2(BDC)_2DABCO$ exposed to 50% RH, the shift of the (010) reflection to higher 2θ values indicates the partial hydrolysis of the framework as previously described.[27] However, the co-presence of vibrational bands that can be ascribed to $Cu_2(BDC)_2DABCO$ and $Cu_2(BDC)_2$, indicates that at 50% RH the MOF-to-MOF transformation is incomplete. In contrast, when $Cu_2(BDC)_2DABCO$ is exposed to 80% RH or liquid water, the final diffraction patterns and IR spectra match those of pure $Cu_2(BDC)_2$, suggesting a complete transformation from the pillar-layered MOF to the 2D framework. We note that there is an emerging research in the synthesis of MOF superstructures;[16,17,37] for example, it has been demonstrated that a $Zn_2(BDC)_2DABCO$ MOF single crystal can evolve in an iso-oriented MOF superstructure.[48] While in single-crystal transformations, the crystal shape is typically preserved,[49] our SEM data indicates that the initial $Cu_2(BDC)_2DABCO$ crystals are replaced by $Cu_2(BDC)_2$ crystals with different morphology (see RH = 80% Fig. S15†). This morphological change could indicate that the formation of the 2D MOF occurs *via* recrystallization of building units that were initially part of the $Cu_2(BDC)_2DABCO$ framework (Fig. 4c). Considering that DABCO has a water solubility of 61 g/100 g H_2O,[50] whereas H_2BDC is rather insoluble,[51] it is expected to have a high concentration of BDC, originated from the dissolution of the original framework, available for recrystallization. On the other hand, after hydrolysis of the coordination bonds, DABCO is expected to be easily removed from the framework. This hypothesis is confirmed by the absence of the DABCO vibrational bands from $Cu_2(BDC)_2DABCO$ films after exposure to liquid water. We further note that Fischer and co-workers reported that $Cu_2(BDC)_2DABCO$ does not form in the presence of water (40 °C), but the synthesis yields $Cu_2(BDC)_2$ crystals instead.[52] This suggests that, under the investigated humid conditions, the recrystallization of $Cu_2(BDC)_2DABCO$ at room temperature is unlikely while the formation of $Cu_2(BDC)_2$ is favoured.

We hypothesize a second contribution to the growth of $Cu_2(BDC)_2$: by SEM we noted that in the $Cu_2(BDC)_2DABCO$ films, we could observe regions exposing uncoated $Cu(OH)_2$ NBs (Fig. S15†). The presence of these residual NBs in pristine $Cu_2(BDC)_2DABCO$ films was also confirmed by XRD, showing the (021) reflection of $Cu(OH)_2$ in the diffraction pattern. When immersing $Cu_2(BDC)_2DABCO$ films in liquid water, we then observed the formation of plate-like $Cu_2(BDC)_2$ crystallites in these regions of exposed NBs. X-ray diffraction analyses of these films showed that the appearance of $Cu_2(BDC)_2$ was concomitant with a slight decrease of the (021) $Cu(OH)_2$ intensity. This suggests that after degradation of the original framework, $Cu_2(BDC)_2$ could be partially formed from unreacted $Cu(OH)_2$ directly on the NBs.

Overall the data suggest that immersion of $Cu_2(BDC)_2$-DABCO films in water triggers both, a heteroepitaxial transformation into $Cu_2(BDC)_2$ and a fresh heteroepitaxial growth from the exposed $Cu(OH)_2$.

In order to assess how the transformation process influences the overall crystalline orientation of the MOF film, we investigated the azimuthal angle dependence of the intensity of the respective (100) reflections of $Cu_2(BDC)_2DABCO$ and $Cu_2(BDC)_2$ before and after exposure to 80% RH and liquid water. The intensity profile of the as prepared 3D-oriented $Cu_2(BDC)_2$-DABCO film showed two intensity maxima of the (100) reflection at approx. 60° and 240° (Fig. 5a). The (001) planes in the same sample have their maxima shifted by 90°, complying with the tetragonal MOF unit cell[53] and confirming the in-plane order in the as-synthesized film. After exposure to 80% RH, the intensity profile of the (100) reflection ascribed to $Cu_2(BDC)_2$ shows also two intensity maxima shifted by 180° (Fig. 5b); the profile of the (001) reflection confirms the decomposition of $Cu_2(BDC)_2DABCO$ crystals. Similar intensity profiles were observed when $Cu_2(BDC)_2DABCO$ films were immersed in water; however, in this case, a broader distribution of crystalline orientations was recorded (Fig. S17†). Notably, the position of the maxima of the new $Cu_2(BDC)_2$ phase coincides with the maxima of the pristine oriented $Cu_2(BDC)_2DABCO$. This indicates that the (100) planes of $Cu_2(BDC)_2DABCO$ might take an active role in the recrystallization of the 2D MOF layers by directing the growth of $Cu_2(BDC)_2$ during the MOF-to-MOF transformation process. The mechanism could be explained by the lattice match between the two frameworks, which was also recently reported for the epitaxial recrystallization of oriented MOF nanostructures from a labile Cu-MOF single crystal.[37] This epitaxial recrystallization from 3D-oriented $Cu_2(BDC)_2DABCO$ films to $Cu_2(BDC)_2$ coatings, here supported by chemical, structural and morphological investigations, is the first evidence that an oriented MOF superstructure could be transformed into an iso-oriented, chemically and structurally distinct MOF superstructure. To further examine the kinetics and morphological changes of this process, we performed additional *in situ* experiments (*vide infra*).

For the heteroepitaxially grown $Cu_2(BPDC)_2DABCO$ MOF film exposed to 50% RH, the crystallinity also decreased significantly within the initial 24 h, suggesting the hydrolysis of the network. However, this drop is not as drastic as for $Cu_2(BDC)_2DABCO$ under the same environmental condition ($Cu_2(BDC)_2DABCO$: 90% drop of the signal after 24 h at 50% RH), consistent with the hypothesis that higher relative humidity is needed to effectively displace the linkers in MOFs with larger pore sizes. Interestingly, the IR spectra of exposed $Cu_2(BPDC)_2DABCO$ films show the appearance of vibrational bands that could be ascribed to the presence of $Cu_2(BPDC)_2$. This suggests that during the storage in humid environments, the crystalline $Cu_2(BPDC)_2DABCO$ 3D framework tends to evolve into a $Cu_2(BPDC)_2$ 2D network. A transformation mechanism similar to that of $Cu_2(BDC)_2DABCO$ seems

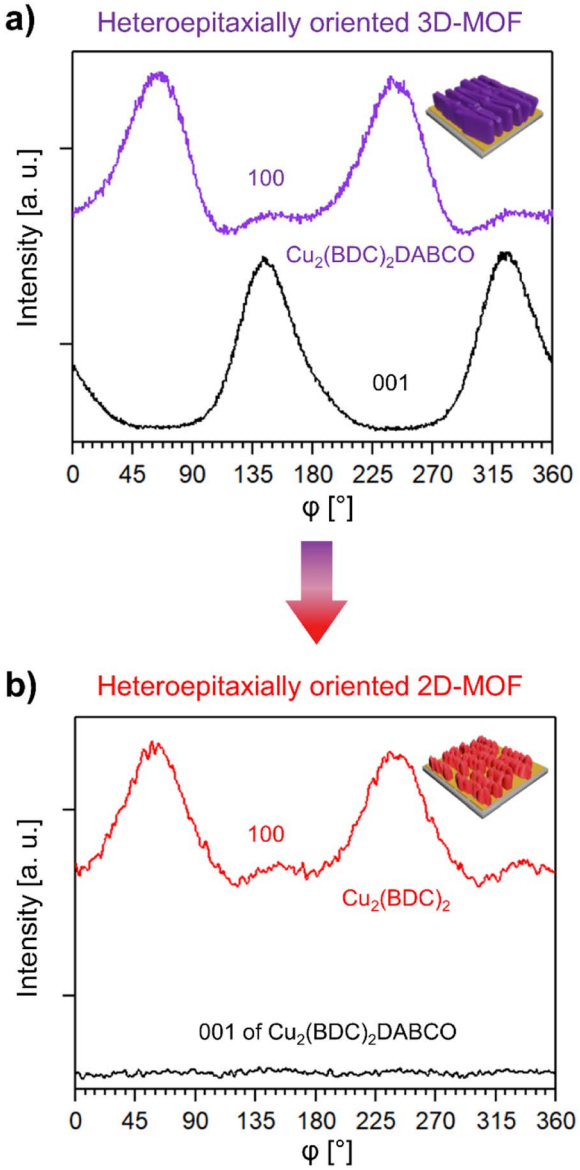

Fig. 5 (a) Azimuthal intensity profile of the (100) and (001) reflection of $Cu_2(BDC)_2DABCO$ before exposure to 80% RH, (b) azimuthal intensity profile of the (100) reflection of newly formed $Cu_2(BDC)_2$ after exposure to 80% RH and of the (001) reflection of $Cu_2(BDC)_2DABCO$, confirming the absence of the DABCO pillar ligand. The average intensity of the (001) reflection of $Cu_2(BDC)_2DABCO$ in (b) is similar to the lowest intensity measured in the azimuthal scan of $Cu_2(BDC)_2$ (see Fig. S17† for plots with intensities).

plausible due to the low water-solubility of the BPDC linker. However, unlike the previously described MOF-to-MOF transformation with BDC, the XRD diffraction patterns show minimal crystallinity with increasing water loading (Fig. S6†). This is consistent with the SEM micrographs, which show how $Cu_2(BPDC)_2DABCO$ crystals progressively lose their sharp crystal edges and holes appear on the crystal surface (Fig. S16†); this morphological change is typically indicative of degradation by-products with low crystallinity.[33,54]

Time-resolved analysis of the heteroepitaxial MOF-to-MOF transformation

In situ methods are a potent tool to investigate the formation, growth, and decomposition of MOFs.[55] For example, time-resolved XRD was used to understand defect formation in pillar-layered $Zn_2(BDC\text{-}TM)_2DABCO$ under humid environments,[56] and *in situ* single crystal XRD revealed mechanistic aspects of the water sorption of Y-shp-MOF-5.[57] Using synchrotron scattering techniques, the structural changes in the framework can be observed with a time resolution as small as 100 ms, revealing important kinetic information about MOF growth or degradation.[58–60] We note that small angle X-ray scattering (SAXS) was used to understand the decomposition of HKUST-1 under controlled humidity.[61] Inspired by these works, we used grazing incidence wide angle X-ray scattering (GIWAXS) to perform time-resolved studies on $Cu_2(BDC)_2DABCO$ films and elucidate the epitaxial recrystallization into $Cu_2(BDC)_2$.

High-resolution GIWAXS patterns were recorded using a humidity chamber set at 50% RH, 80% RH, and increasing humidity from 5–90% RH. For these *in situ* studies, a time resolution of 60 s between the acquisition of the diffractograms was selected. Additionally, we monitored the transformation of $Cu_2(BDC)_2DABCO$ films immersed in water, using a customized chemical cell at an increased time resolution of 1.1 s. For data analysis, we considered the out-of-plane component of the collected 2D images to monitor the (010) reflection of $Cu_2(BDC)_2DABCO$, and the (001) reflection of $Cu_2(BDC)_2$, and correlated the structural changes to the water loading during the *in situ* measurements. Since the *d*-spacing of the investigated reflections of the 3D and 2D framework is similar (1.08 nm for $Cu_2(BDC)_2DABCO$, and 1.05 nm for $Cu_2(BDC)_2$), the collected reflections partially overlap. To selectively follow the degradation of oriented $Cu_2(BDC)_2DABCO$ crystals, we also monitored the (110) reflection (Fig. S4†). In addition, to examine the role of $Cu(OH)_2$ in the transformation process, we monitored the (021) reflection ((021) does not overlap with second order reflections from $Cu_2(BDC)_2DABCO$ or $Cu_2(BDC)_2$ in the region at 11.5 nm^{-1}).

The time-resolved data reveals that the transformation of $Cu_2(BDC)_2DABCO$ to $Cu_2(BDC)_2$ is highly dependent on the applied water loadings. GIWAXS data show that up to 50% RH, diffraction patterns remain identical to the as-synthesized sample (Fig. S18†), indicating water-stability up to this humidity value. However, once 50% RH is reached, the intensities of the (010) and (110) $Cu_2(BDC)_2DABCO$ reflections rapidly drop and shift to higher *q* values (Fig. S18 and S19†). The shift was previously observed by Chabal and co-workers with a laboratory X-ray diffractometer and attributed to the partial hydrolysis of $Cu_2(BDC)_2DABCO$ powder exposed to 50% RH.[27] In our GIWAXS investigation, from 50% to 70% RH, the intensity and the *d*-spacing of the diffraction signal further decreases, indicating enhanced sensitivity towards higher water contents after this intermediate stage (Fig. S19†). Between 70% and 80% RH, the (110) reflection of $Cu_2(BDC)_2DABCO$ eventually disappears and only the diffraction pattern of $Cu_2(BDC)_2$ remains (Fig. 6a, S19,

and Movie S1†), suggesting the end of the heteroepitaxial conversion from $Cu_2(BDC)_2DABCO$ to $Cu_2(BDC)_2$. The integrated intensity of the (010)-(001) region and the (110) reflection of $Cu_2(BDC)_2DABCO$ over the whole experiment time span reveals that the transformation is not a linear process, and it occurs in two steps (Fig. 6b). At 50% RH, an initial sharp decline can be ascribed to the partial hydrolysis of the MOF.[27] However, the (110) plateaus until 70–80% RH, where a second abrupt decline of intensity evidences a significant degradation of the remaining 3D framework. Due to the overlapping signals of $Cu_2(BDC)_2DABCO$ and $Cu_2(BDC)_2$ in the region between 5.6 and 6.4 nm^{-1}, this second step could not be observed for the (010) reflection and it is notably difficult to assess when the formation of the 2D framework takes place. However, by plotting the peak position maxima of the (010)-(001) reflection range *versus* the applied humidity, the two-step mechanism is also evident (Fig. 6c). In accordance with the integrated intensity profile of the (110) reflection of $Cu_2(BDC)_2$-DABCO, the first step takes place at 50% RH, showing a shift from 5.81 nm^{-1} to 5.89 nm^{-1}, which is consistent with the previously reported increase of the (010) interlayer distance caused by the partial hydrolysis of the 3D-framework.[27] The second shift in the *q*-value at 70–80% RH can then be attributed to the recrystallization of the $Cu_2(BDC)_2$ film upon dissolution of the DABCO ligand. When RH is increased by 10% min^{-1} and held at a target value of 80%, the transformation to $Cu_2(BDC)_2$ is complete within 20 min (Fig. S20†). Under immersion in water, the kinetics of the process

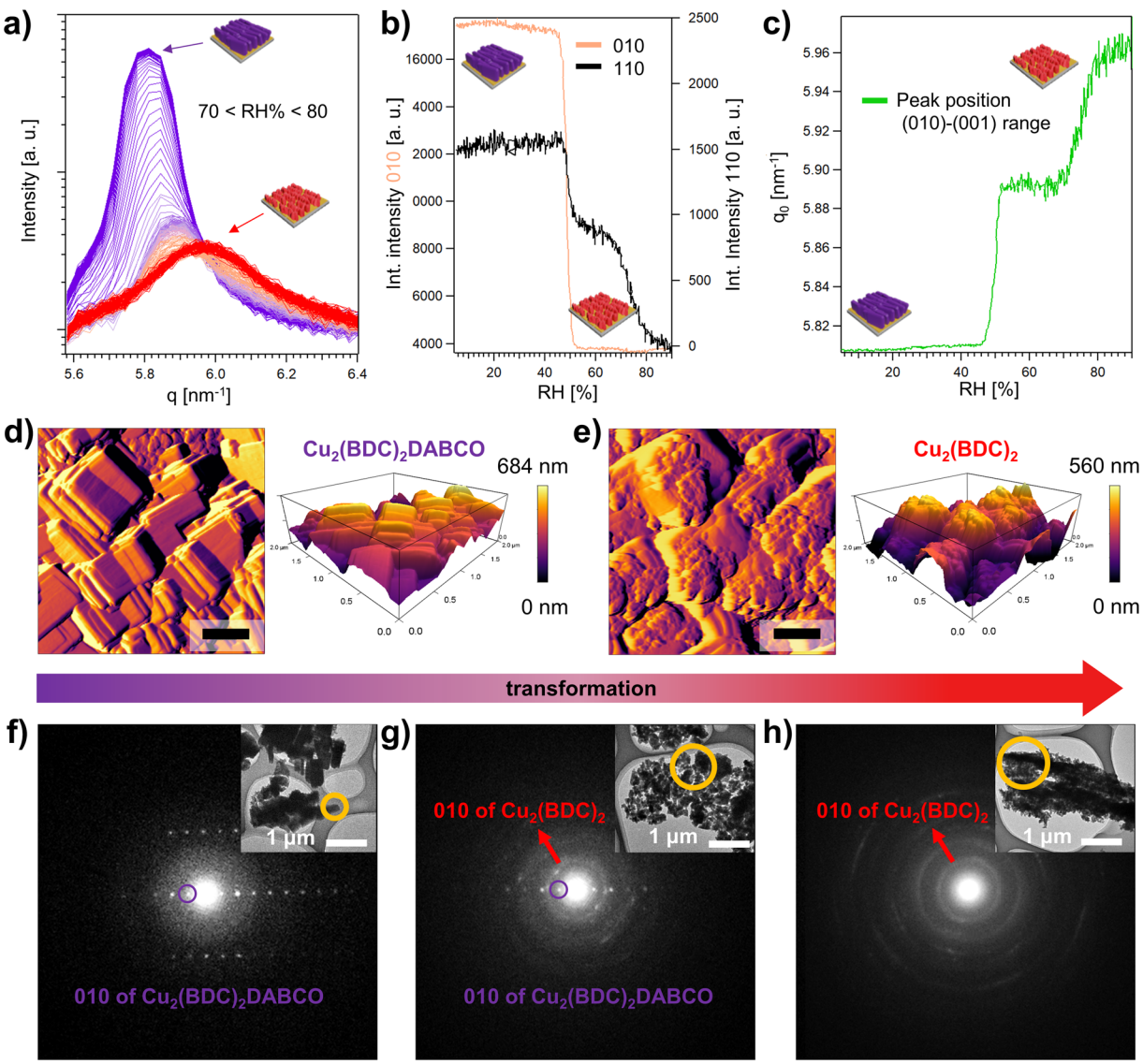

Fig. 6 (a) Time-resolved GIWAXS data showing the transformation of the $Cu_2(BDC)_2DABCO$ film to $Cu_2(BDC)_2$ in the region of the (010)-(001) reflections of the two frameworks, (b) integrated intensity of the (010) and (110) reflections of $Cu_2(BDC)_2DABCO$ with increasing relative humidity, (c) peak position q_0 of the (010)-(001) signal range plotted *versus* the applied relative humidity during the GIWAXS measurement, (d) AFM amplitude and 3D topography image of $Cu_2(BDC)_2DABCO$ collected in tapping mode before exposure to humid Ar flow, (e) AFM amplitude and 3D topography image of the same sample after exposure to humid Ar flow (80% RH) for 100 min. Scale bars represent 400 nm. Electron diffraction patterns of (f) pristine $Cu_2(BDC)_2DABCO$, (g) $Cu_2(BDC)_2DABCO$ exposed to 80% RH for 10 min, showing the beginning of the MOF-to-MOF transformation, and (h) transformed $Cu_2(BDC)_2$ (in 80% RH for 3 h).

is faster and it takes only a few seconds (Fig. S21†). This suggests that, under these conditions, the coordination bonds of Cu_2(BDC)$_2$DABCO are almost instantly broken. When examining the $Cu(OH)_2$ patterns, we note that the signal assigned to the (021) reflection of $Cu(OH)_2$ remains unchanged up to 50% RH, and shows only a slight decrease in intensity for higher RH values including liquid water (Fig. S18–20†). This slight consumption of the residual metal hydroxide concomitant to the formation of $Cu_2(BDC)_2$ suggests a partial heteroepitaxial growth process on aligned $Cu(OH)_2$ nanobelts.

High magnification SEM micrographs recorded after the *in situ* experiment at 50% RH show crystals of Cu_2(BDC)$_2$DABCO with rounded corners and soft edges, which is in accordance with the reduced crystallinity observed for this intermediate stage of the transformation process (Fig. S22†). In contrast, after exposure to 80% RH for 30 min, the previously described regions of concentrated polycrystalline $Cu_2(BDC)_2$ were observed while the surrounding $Cu(OH)_2$ nanostructures seemed mostly unaffected (Fig. S23†). In case of exposure of Cu_2(BDC)$_2$DABCO to liquid water, the images show densely populated regions surrounded by single $Cu_2(BDC)_2$ particles on the previously unreacted $Cu(OH)_2$ NBs (Fig. S24†). These results are consistent with the previously recorded SEM micrographs (*vide supra*). SEM-EDX analysis, comparing pristine Cu_2(BDC)$_2$DABCO and $Cu_2(BDC)_2$ after transformation at 80% RH, shows that nitrogen is effectively removed in the transformed film. This indicates that DABCO is indeed released from the framework and its sublimation[62] is enhanced under high-vacuum conditions during the SEM-EDX measurement (Fig. S25†).

To further examine the morphological changes during the heteroepitaxial transformation from Cu_2(BDC)$_2$DABCO to $Cu_2(BDC)_2$, time-resolved AFM measurements were performed in a small environmental chamber under humid Ar flow (80% RH at exit of the chamber). The *in situ* morphological analysis revealed that within a few minutes in humid conditions, terrace-like steps and rounded crystal corners appear, indicating a degradation of the original cuboid morphology for the Cu_2(BDC)$_2$DABCO film. Over time (Fig. 6d, e, S26, and Movie S2†), we observed the formation of the plate-like morphology of $Cu_2(BDC)_2$, which preferentially grows in an ordered fashion, spreading from Cu_2(BDC)$_2$DABCO crystal edges towards the centre of the crystal faces. The higher reactivity of crystal edges was previously noticed and ascribed to a higher concentration of defects.[63] During the transformation, the crystallite size changed from approx. 530 × 290 nm (initial Cu_2(BDC)$_2$DABCO) to 110 × 80 nm (transformed $Cu_2(BDC)_2$) (Table S1†). In addition to this, 3D AFM topography images show that the maximum height of 648 nm of the Cu_2(BDC)$_2$DABCO film is reduced to 560 nm after exposure to 80% RH for 100 min (Fig. 6d, e). This decrease in the film thickness can be attributed to partial material loss or vertical contraction as the initial framework progressively transforms from the surface towards underlying layers. Similar changes in film thickness were estimated from SEM micrographs recorded at a 45° tilting angle (Fig. S27†).

To validate the phase transition from Cu_2(BDC)$_2$DABCO to $Cu_2(BDC)_2$, selected area electron diffraction (SAED) was used to analyse the nanocrystals scratched from the Si substrates. For a single pristine Cu_2(BDC)$_2$DABCO crystallite, the obtained electron diffraction pattern revealed sharp spots (Fig. 6f) with a calculated *d*-value of $d_{010} = 1.08$ nm, which agrees well with our PXRD data (d = 1.08 nm) and the reported crystal structure of the MOF.[20,53] Then, to access the intermediate stage of the transformation, a Cu_2(BDC)$_2$DABCO film was exposed to 80% RH for 10 min, solvent-exchanged to dichloromethane, evacuated, and stored under inert conditions (Ar) until measurement. The electron diffraction of this sample shows the previously described diffraction spots of the Cu_2(BDC)$_2$DABCO phase ($d_{010} = 1.08$ nm) as well as broad diffraction rings attributed to $Cu_2(BDC)_2$, indicating the co-existence of both MOF phases (Fig. 6g). The diffraction rings consist of overlapping diffraction spots, which can be attributed to the electron diffraction from multiple $Cu_2(BDC)_2$ crystallites being included in the selected area. The calculated *d*-value of $d_{010} = 0.59$ nm corresponds to that of reported $Cu_2(BDC)_2$.[19] For the film exposed to 80% RH for 3 h, the electron diffraction pattern shows only diffraction rings of $Cu_2(BDC)_2$ ($d_{010} = 0.59$ nm), confirming the complete MOF-to-MOF transformation in the crystal phases (Fig. 6h).

In order to determine how the MOF-to-MOF transformation influences the porosity of the different frameworks, powdery Cu_2(BDC)$_2$DABCO was exposed to H_2O and the formation of the 2D framework confirmed by PXRD (Fig. S28†). N_2 adsorption isotherms then revealed that the transformed $Cu_2(BDC)_2$ shows similar properties as pristine $Cu_2(BDC)_2$, with BET surface areas of 160 $m^2\ g^{-1}$ and 145 $m^2\ g^{-1}$, respectively (Fig. S28†).

Overall, these changes observed in morphology, *in situ* X-ray scattering, and electron diffraction demonstrate that at 80% RH the transformation from Cu_2(BDC)$_2$DABCO films to $Cu_2(BDC)_2$ occurs preferentially *via* a dissolution and recrystallization pathway. The time-resolved experiments further demonstrate that a 3D-ordered MOF superstructure can undergo a heteroepitaxial recrystallization mechanism.

Conclusions

In this study, we investigated the structural stability of heteroepitaxially grown MOF films in environments ranging from 50% RH to liquid H_2O. We found that the 2D frameworks $Cu_2(BDC)_2$ and $Cu_2(BPDC)_2$, organized as 3D-oriented polycrystalline MOF films, maintain their crystallinity, chemical composition and morphology at all water loadings. This stability in environmental conditions is desirable for applications of oriented MOF films in functional devices. For the pillar-layered 3D frameworks, Cu_2(BDC)$_2$DABCO and Cu_2(BPDC)$_2$DABCO, the related oriented MOF films undergo significant degradation and morphological changes even in milder environments of 50% RH. We ascribed this water sensitivity to the increased water transfer *via* the MOF voids that have larger out-of-plane pore apertures. Thus, for practical applications of these 3D-ordered films, protection from humidity is required. Preservation strategies[64,65] could involve the design of MOFs with enhanced hydrophobic properties,[66,67] the deposition of hydrophobic coatings,[68] or the utilization of protective vacuum cases.[69]

While the degradation product of Cu_2(BPDC)$_2$DABCO was found to be amorphous, we observed conditions (*i.e.* RH >

70%) in which an ordered film of $Cu_2(BDC)_2DABCO$ transforms into an ordered film of $Cu_2(BDC)_2$. By combining time-resolved synchrotron experiments and *in situ* AFM measurements, we identified salient aspects of the transformation mechanism, including the hydrolysis of the original framework and the recrystallization of the building blocks as an oriented 2D MOF coating. The recrystallization was demonstrated to follow a heteroepitaxial pathway. These results highlight that in conditions that allow a MOF-to-MOF transformation, an original organization of crystals in a 3D-oriented superstructure could lead to oriented, but distinct polycrystalline MOF systems. Our results suggest that the conversion among 3D-oriented superstructures could be a valuable alternative synthetic approach for the fabrication of oriented MOF films.

Author contributions

L. A. B.: design of methodology, MOF synthesis, curation, writing – original draft; M. L.-M.: design of methodology, AFM and Raman measurements, writing – review & editing; G. Z. and Z. H.: TEM measurements, editing; H. A.: supervision GIWAXS measurements, technical support and analysis; S. D.-Z.: SEM and EDX measurements; C. D.: validation, writing – review & editing; P. F.: design of methodology, supervision, validation, writing – review & editing, funding acquisition.

Conflicts of interest

There are no conflicts to declare.

Acknowledgements

The authors are thankful for the support of M. de J. Velásquez-Hernández and V. Lipic during the synchrotron beam time (GIWAXS measurements) and M. de J. Velásquez-Hernández for her help with N_2 adsorption measurements. The authors thank Behnaz Abbasgholi_NA for her support in SEM imaging. The authors acknowledge support from the European Research Council under the European Union's Horizon 2020 Programme (FP/2014-2020)/ERC Grant Agreement No. 771834—POPCRYSTAL and the TU Graz for the Lead Project (No. LP-03). G. Z. and Z. H. acknowledge support from the Swedish research council FORMAS (2020-00831) and the Swedish research council VR (2022-02939). The authors acknowledge the CERIC-ERIC Consortium for the access to the Austrian SAXS beamline experimental facilities at Elettra Synchrotron and financial support. The authors thank Masahide Takahashi and Kenji Okada for fruitful discussions.

Notes and references

1 H. Furukawa, K. E. Cordova, M. O'Keeffe and O. M. Yaghi, *Science*, 2013, **341**, 1230444.
2 S. Kitagawa, R. Kitaura and S. Noro, *Angew. Chem., Int. Ed.*, 2004, **43**, 2334–2375.
3 X. Zhang, Z. Chen, X. Liu, S. L. Hanna, X. Wang, R. Taheri-Ledari, A. Maleki, P. Li and O. K. Farha, *Chem. Soc. Rev.*, 2020, **49**, 7406–7427.
4 L. S. Xie, G. Skorupskii and M. Dincă, *Chem. Rev.*, 2020, **120**, 8536–8580.
5 G. M. Espallargas and E. Coronado, *Chem. Soc. Rev.*, 2018, **47**, 533–557.
6 C. Cong and H. Ma, *Adv. Opt. Mater.*, 2021, **9**, 2100733.
7 P. Falcaro, R. Ricco, C. M. Doherty, K. Liang, A. J. Hill and M. J. Styles, *Chem. Soc. Rev.*, 2014, **43**, 5513–5560.
8 J. Liu and C. Wöll, *Chem. Soc. Rev.*, 2017, **46**, 5730–5770.
9 L. Pilz, C. Natzeck, J. Wohlgemuth, N. Scheuermann, P. G. Weidler, I. Wagner, C. Wöll and M. Tsotsalas, *Adv. Mater. Interfaces*, 2023, **10**, 2201771.
10 O. Dalstein, E. Gkaniatsou, C. Sicard, O. Sel, H. Perrot, C. Serre, C. Boissière and M. Faustini, *Angew. Chem., Int. Ed.*, 2017, **56**, 14011–14015.
11 O. Dalstein, D. R. Ceratti, C. Boissière, D. Grosso, A. Cattoni and M. Faustini, *Adv. Funct. Mater.*, 2016, **26**, 81–90.
12 M. Krishtab, I. Stassen, T. Stassin, A. J. Cruz, O. O. Okudur, S. Armini, C. Wilson, S. De Gendt and R. Ameloot, *Nat. Commun.*, 2019, **10**, 3729.
13 W. Zhan, Q. Kuang, J. Zhou, X. Kong, Z. Xie and L. Zheng, *J. Am. Chem. Soc.*, 2013, **135**, 1926–1933.
14 I. E. Khalil, J. Fonseca, M. R. Reithofer, T. Eder and J. M. Chin, *Coord. Chem. Rev.*, 2023, **481**, 215043.
15 J. Fonseca, L. Meng, I. Imaz and D. Maspoch, *Chem. Soc. Rev.*, 2023, **52**, 2528–2543.
16 C. Avci, I. Imaz, A. Carné-Sánchez, J. A. Pariente, N. Tasios, J. Pérez-Carvajal, M. I. Alonso, A. Blanco, M. Dijkstra, C. López and D. Maspoch, *Nat. Chem.*, 2018, **10**, 78–84.
17 F. Cheng, A. J. Young, J.-S. G. Bouillard, N. T. Kemp, R. Guillet-Nicolas, C. H. Hall, D. Roberts, A. H. Jaafar, A. M. Adawi, F. Kleitz, A. Imhof, M. R. Reithofer and J. M. Chin, *J. Am. Chem. Soc.*, 2019, **141**, 12989–12993.
18 P. I. Scheurle, A. Mähringer, A. Biewald, A. Hartschuh, T. Bein and D. D. Medina, *Chem. Mater.*, 2021, **33**, 5896–5904.
19 P. Falcaro, K. Okada, T. Hara, K. Ikigaki, Y. Tokudome, A. W. Thornton, A. J. Hill, T. Williams, C. Doonan and M. Takahashi, *Nat. Mater.*, 2017, **16**, 342–348.
20 K. Okada, M. Nakanishi, K. Ikigaki, Y. Tokudome, P. Falcaro, C. J. Doonan and M. Takahashi, *Chem. Sci.*, 2020, **11**, 8005–8012.
21 M. de J. Velásquez-Hernández, M. Linares-Moreau, L. A. Brandner, B. Marmiroli, M. Barella, G. P. Acuna, S. D. Zilio, M. F. K. Verstreken, D. E. Kravchenko, O. M. Linder-Patton, J. D. Evans, H. Wiltsche, F. Carraro, H. Wolinski, R. Ameloot, C. Doonan and P. Falcaro, *Adv. Mater.*, 2023, **35**, 2211478.
22 A. Tarzia, M. Takahashi, P. Falcaro, A. W. Thornton, C. J. Doonan and D. M. Huang, *ACS Appl. Mater. Interfaces*, 2018, **10**, 40938–40950.
23 M. Linares-Moreau, L. A. Brandner, T. Kamencek, S. Klokic, F. Carraro, K. Okada, M. Takahashi, E. Zojer, C. J. Doonan and P. Falcaro, *Adv. Mater. Interfaces*, 2021, **8**, 2101039.

24 B. Baumgartner, R. Mashita, A. Fukatsu, K. Okada and M. Takahashi, *Angew. Chem., Int. Ed.*, 2022, **61**, e202201725.
25 K. Okada, R. Mashita, A. Fukatsu and M. Takahashi, *Nanoscale Adv.*, 2023, **5**, 1795–1801.
26 S. Klokic, D. Naumenko, B. Marmiroli, F. Carraro, M. Linares-Moreau, S. D. Zilio, G. Birarda, R. Kargl, P. Falcaro and H. Amenitsch, *Chem. Sci.*, 2022, **13**, 11869–11877.
27 K. Tan, N. Nijem, P. Canepa, Q. Gong, J. Li, T. Thonhauser and Y. J. Chabal, *Chem. Mater.*, 2012, **24**, 3153–3167.
28 N. C. Burtch, H. Jasuja and K. S. Walton, *Chem. Rev.*, 2014, **114**, 10575–10612.
29 X. Liu, X. Wang and F. Kapteijn, *Chem. Rev.*, 2020, **120**, 8303–8377.
30 M. E. A. Safy, M. Amin, R. R. Haikal, B. Elshazly, J. Wang, Y. Wang, C. Wöll and M. H. Alkordi, *Chem. – Eur. J.*, 2020, **26**, 7109–7117.
31 C. Li, A. Chandresh, Z. Zhang, S. Moulai and L. Heinke, *Adv. Mater. Interfaces*, 2022, **9**, 2101947.
32 M. Todaro, G. Buscarino, L. Sciortino, A. Alessi, F. Messina, M. Taddei, M. Ranocchiari, M. Cannas and F. M. Gelardi, *J. Phys. Chem. C*, 2016, **120**, 12879–12889.
33 M. P. Singh, N. R. Dhumal, H. J. Kim, J. Kiefer and J. A. Anderson, *J. Phys. Chem. C*, 2016, **120**, 17323–17333.
34 S. S.-Y. Chui, S. M.-F. Lo, J. P. H. Charmant, A. G. Orpen and I. D. Williams, *Science*, 1999, **283**, 1148–1150.
35 C. Huang, J. Dong, W. Sun, Z. Xue, J. Ma, L. Zheng, C. Liu, X. Li, K. Zhou, X. Qiao, Q. Song, W. Ma, L. Zhang, Z. Lin and T. Wang, *Nat. Commun.*, 2019, **10**, 2779.
36 D. Saha and S. Deng, *J. Phys. Chem. Lett.*, 2010, **1**, 73–78.
37 L. Shao, F. Meng, J. Chen and Y. Fu, *J. Mater. Chem. A*, 2023, **11**, 5027–5036.
38 H. Amenitsch, M. Rappolt, M. Kriechbaum, H. Mio, P. Laggner and S. Bernstorff, *J. Synchrotron Radiat.*, 1998, **5**, 506–508.
39 B. Marmiroli, B. Sartori, A. R. Kyvik, I. Ratera and H. Amenitsch, *Front. Mater.*, 2021, **8**, 686353.
40 M. Bogar, I. Khalakhan, A. Gambitta, Y. Yakovlev and H. Amenitsch, *J. Power Sources*, 2020, **477**, 229030.
41 J. Razjouyan, H. Lee, B. Gilligan, C. Lindberg, H. Nguyen, K. Canada, A. Burton, A. Sharafkhaneh, K. Srinivasan, F. Currim, S. Ram, M. R. Mehl, N. Goebel, M. Lunden, S. Bhangar, J. Heerwagen, K. Kampschroer, E. M. Sternberg and B. Najafi, *Indoor Air*, 2020, **30**, 167–179.
42 T. Truong, K. D. Nguyen, S. H. Doan and N. T. S. Phan, *Appl. Catal., A*, 2016, **510**, 27–33.
43 V. I. Kovalenko, A. A. Akhmadiyarov, A. E. Vandyukov and A. R. Khamatgalimov, *J. Mol. Struct.*, 2012, **1028**, 134–140.
44 P. Guo, D. Dutta, A. G. Wong-Foy, D. W. Gidley and A. J. Matzger, *J. Am. Chem. Soc.*, 2015, **137**, 2651–2657.
45 K. Seki and W. Mori, *J. Phys. Chem. B*, 2002, **106**, 1380–1385.
46 B. Liu, M. Tu and R. A. Fischer, *Angew. Chem., Int. Ed.*, 2013, **52**, 3402–3405.
47 A. Bétard, S. Wannapaiboon and R. A. Fischer, *Chem. Commun.*, 2012, **48**, 10493–10495.
48 Z. Chen, S. Xiang, D. Zhao and B. Chen, *Cryst. Growth Des.*, 2009, **9**, 5293–5296.
49 X.-J. Bai, X. Zhai, L.-Y. Zhang, Y. Fu and W. Qi, *Matter*, 2021, **4**, 2919–2935.
50 A. Farkas, G. A. Mills, W. E. Erner and J. B. Maerker, *J. Chem. Eng. Data*, 1959, **4**, 334–335.
51 N. Han, L. Zhu, L. Wang and R. Fu, *Sep. Purif. Technol.*, 1999, **16**, 175–180.
52 Z. Wang, K. Rodewald, R. Medishetty, B. Rieger and R. A. Fischer, *Cryst. Growth Des.*, 2018, **18**, 7451–7459.
53 Y. Kim, R. Haldar, H. Kim, J. Koo and K. Kim, *Dalton Trans.*, 2016, **45**, 4187–4192.
54 J.-S. Choi, W.-J. Son, J. Kim and W.-S. Ahn, *Microporous Mesoporous Mater.*, 2008, **116**, 727–731.
55 M. J. Van Vleet, T. Weng, X. Li and J. R. Schmidt, *Chem. Rev.*, 2018, **118**, 3681–3721.
56 N. C. Burtch, I. M. Walton, J. T. Hungerford, C. R. Morelock, Y. Jiao, J. Heinen, Y.-S. Chen, A. A. Yakovenko, W. Xu, D. Dubbeldam and K. S. Walton, *Nat. Chem.*, 2020, **12**, 186–192.
57 R. G. AbdulHalim, P. M. Bhatt, Y. Belmabkhout, A. Shkurenko, K. Adil, L. J. Barbour and M. Eddaoudi, *J. Am. Chem. Soc.*, 2017, **139**, 10715–10722.
58 F. Carraro, J. D. Williams, M. Linares-Moreau, C. Parise, W. Liang, H. Amenitsch, C. Doonan, C. O. Kappe and P. Falcaro, *Angew. Chem., Int. Ed.*, 2020, **59**, 8123–8127.
59 M. de J. Velásquez-Hernández, R. Ricco, F. Carraro, F. T. Limpoco, M. Linares-Moreau, E. Leitner, H. Wiltsche, J. Rattenberger, H. Schröttner, P. Frühwirt, E. M. Stadler, G. Gescheidt, H. Amenitsch, C. J. Doonan and P. Falcaro, *CrystEngComm*, 2019, **21**, 4538–4544.
60 E. Zanchetta, L. Malfatti, R. Ricco, M. J. Styles, F. Lisi, C. J. Coghlan, C. J. Doonan, A. J. Hill, G. Brusatin and P. Falcaro, *Chem. Mater.*, 2015, **27**, 690–699.
61 N. Al-Janabi, A. Alfutimie, F. R. Siperstein and X. Fan, *Front. Chem. Sci. Eng.*, 2016, **10**, 103–107.
62 D. I. Bugaenko, A. V. Karchava and M. A. Yurovskaya, *Chem. Heterocycl. Compd.*, 2020, **56**, 128–144.
63 Z. Gu, W. Zhang, T. Pan, Y. Shen, P. Qin, P. Zhang, X. Li, L. Liu, L. Li, Y. Fu, W. Zhang and F. Huo, *Research*, 2021, **2021**, 854946.
64 M. Ding, X. Cai and H.-L. Jiang, *Chem. Sci.*, 2019, **10**, 10209–10230.
65 K. Jayaramulu, F. Geyer, A. Schneemann, Š. Kment, M. Otyepka, R. Zboril, D. Vollmer and R. A. Fischer, *Adv. Mater.*, 2019, **31**, 1900820.
66 J. Yang, A. Grzech, F. M. Mulder and T. J. Dingemans, *Chem. Commun.*, 2011, **47**, 5244–5246.
67 J. M. Taylor, R. Vaidhyanathan, S. S. Iremonger and G. K. H. Shimizu, *J. Am. Chem. Soc.*, 2012, **134**, 14338–14340.
68 J. Castells-Gil, F. Novio, N. M. Padial, S. Tatay, D. Ruíz-Molina and C. Martí-Gastaldo, *ACS Appl. Mater. Interfaces*, 2017, **9**, 44641–44648.
69 Q. Zhao, F. Carrascoso, P. Gant, T. Wang, R. Frisenda and A. Castellanos-Gomez, *J. Phys.: Mater.*, 2020, **3**, 036001.